

AEDR: Training-Free AI-Generated Image Attribution via Autoencoder Double-Reconstruction

Chao Wang^{1,*}, Zijin Yang¹, Yaofei Wang², Weiming Zhang¹, Kejiang Chen^{1,†}

¹Anhui Province Key Laboratory of Digital Security, University of Science and Technology of China

²Hefei University of Technology

chaowang0708@mail.ustc.edu.cn, bsmhmlf@mail.ustc.edu.cn, wyf@hfut.edu.cn, zhangwm@ustc.edu.cn, chenkj@ustc.edu.cn

Abstract

The rapid advancement of image-generation technologies has made it possible for anyone to create photorealistic images using generative models, raising significant security concerns. To mitigate malicious use, tracing the origin of such images is essential. Reconstruction-based attribution methods offer a promising solution, but they often suffer from reduced accuracy and high computational costs when applied to state-of-the-art (SOTA) models. To address these challenges, we propose AEDR (AutoEncoder Double-Reconstruction), a novel training-free attribution method designed for generative models with continuous autoencoders. Unlike existing reconstruction-based approaches that rely on the value of a single reconstruction loss, AEDR performs two consecutive reconstructions using the model’s autoencoder, and adopts the ratio of these two reconstruction losses as the attribution signal. This signal is further calibrated using the image homogeneity metric to improve accuracy, which inherently cancels out absolute biases caused by image complexity, with autoencoder-based reconstruction ensuring superior computational efficiency. Experiments on eight top latent diffusion models show that AEDR achieves 25.5% higher attribution accuracy than existing reconstruction-based methods, while requiring only 1% of the computational time.

Code — <https://github.com/wangchao0708/AEDR>

1 Introduction

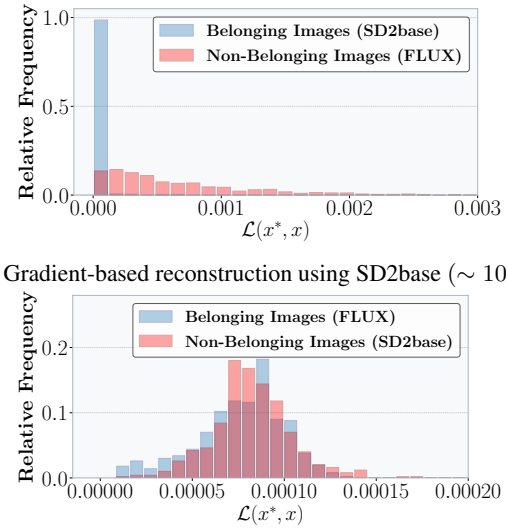
Latent diffusion models (Podell et al. 2023; Batifol et al. 2025; Rombach et al. 2022; Razzhigaev et al. 2023) have emerged as the dominant paradigm in image generation due to their exceptional capabilities in producing high-resolution and photorealistic content. Their effectiveness in modeling complex data distributions has facilitated numerous applications across diverse fields, such as digital art, advertising, and virtual reality (Dhariwal and Nichol 2021). Recent models such as Stable Diffusion 3.5 (Esser et al. 2024) and FLUX.1-dev enable rapid and controllable image synthesis, supporting a wide range of real-world applications.

While the powerful capabilities of AI-generated images are widely embraced, concerns about potential misuse are

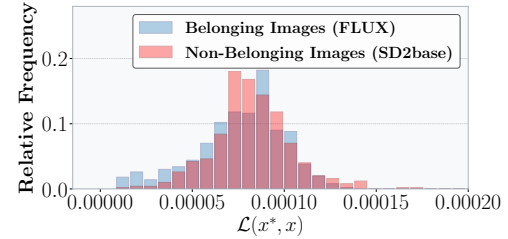
^{*}Work partially done during the internship at iFLYTEK.

[†]Corresponding author.

Copyright © 2026, Association for the Advancement of Artificial Intelligence (www.aaai.org). All rights reserved.



(a) Gradient-based reconstruction using SD2base ($\sim 10^{-4}$).



(b) Gradient-based reconstruction using FLUX ($\sim 10^{-5}$).

Figure 1: Gradient-based reconstruction methods exhibit different loss distributions. These differences lead to attribution failures on the latest model, such as FLUX.

growing (Carlini et al. 2023; Chen et al. 2020; Ong et al. 2021; Zhao et al. 2021). For instance, unscrupulous vendors may repurpose outputs from third-party models as their own, falsely promoting model performance and thereby misleading consumers while undermining fair market competition. Furthermore, malicious actors can present outputs from commercial models (Betker et al. 2023) as original creations to gain reputational and financial advantages, flagrantly violating the intellectual property rights of model developers (Li et al. 2024). Therefore, reliable image origin attribution has become indispensable for accurately identifying the responsible entities behind such generated content.

Existing image attribution methods generally fall into three primary categories. Watermark-based methods (Luo et al. 2009; Swanson, Zhu, and Tewfik 1996; Wen et al. 2023; Yang et al. 2024, 2025) embed invisible or semi-visible marks during image generation, enabling attribution through watermark detection. Fingerprint-based methods (Ding, Thakur, and Li 2021; Yu et al. 2020, 2021) intro-

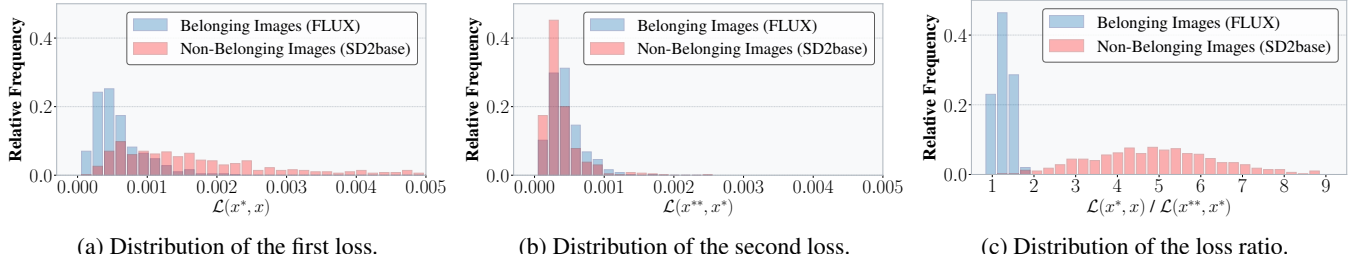


Figure 2: Autoencoder-based double-reconstruction loss variation and loss ratio.

duce model-specific signatures during training or by modifying the architecture, and rely on supervised classifiers to detect these fingerprints in generated images. However, some of these methods may degrade the visual quality of the generated images due to additional operations during training or inference. In contrast, passive detection approaches, which do not require modifications to the training process of target models, are more practical and acceptable in real-world applications. Among these, reconstruction-based methods (Wang et al. 2023, 2024) have achieved excellent performance. They use gradient information from the generative model to reconstruct the input image, with the reconstruction loss between the original and reconstructed images serving as the attribution signal. These methods do not modify model parameters or the generation pipeline, and thus preserve generative performance, making them one of the most promising approaches for image attribution.

Existing gradient-based reconstruction methods typically follow this observation: images that belong to the target model generally exhibit lower reconstruction losses than non-belonging images (see Figure 1a). Thus, the two types of images can be distinguished based on a single reconstruction loss value. However, with increasingly powerful generative models such as FLUX (Batifol et al. 2025), these methods (Wang et al. 2023, 2024) tend to produce extremely low reconstruction losses for both belonging and non-belonging images, causing significant overlap in the loss distributions and thereby reducing attribution accuracy (see Figure 1b). Moreover, the gradient-guided reconstruction process is computationally expensive and complex, making these methods impractical for real-world applications.

To address these limitations, we prefer to adopt autoencoder-based reconstruction as the foundation for an efficient attribution. However, using reconstruction loss directly is susceptible to the inherent complexity of the input image (Choi et al. 2024; Ricker, Lukovnikov, and Fischer 2024): Images with simple textures naturally have lower reconstruction loss, while those with complex textures correspondingly have higher reconstruction loss (Further details are provided in Sections 2 and 3 of the Technical Appendix). To mitigate this bias introduced by image complexity, we propose an attribution method based on the loss ratio across double-reconstructions by the autoencoder. The key insight is that the autoencoder has learned to capture representative features of samples from the training distribution. As illustrated in Figure 2a and Figure 2b, we observe

that when the autoencoder reconstructs a belonging image twice, the resulting reconstruction losses are nearly identical, since the image lies within the model’s distribution. In contrast, for the non-belonging image, which initially lies outside the model distribution, the first reconstruction effectively projects it into the distribution, leading to a noticeably lower loss in the second reconstruction. Given the pronounced disparity, if we compute the ratio of the first to the second reconstruction loss, the value tends to be close to 1 for belonging images, but significantly greater than 1 for non-belonging images (see Figure 2c).

Motivated by this insight, we propose an image attribution method based on **AutoEncoder Double-Reconstruction**, namely **AEDR**. Unlike existing gradient-guided approaches that utilize single reconstruction loss, AEDR employs the loss ratio from double reconstructions, calibrated by an image homogeneity metric. This approach mitigates discrepancies arising from image texture complexity. Additionally, we implement a Kernel Density Estimation method (Kim and Scott 2012) for adaptive threshold selection, which assumes no prior knowledge of underlying data distributions, thereby enhancing the adaptability across diverse generative models. Our contributions are summarized as follows:

- We reveal that existing reconstruction-based image attribution methods, which rely on the single reconstruction loss, face significant challenges when applied to SOTA generative models. We identify a key discrepancy: under autoencoder-based double-reconstruction, belonging images show significantly higher latent feature consistency across reconstructions than non-belonging ones.
- We propose AEDR, an training-free passive attribution method that leverages the ratio of losses from two successive reconstructions and calibrates it based on image homogeneity. AEDR performs direct reconstruction using the model’s autoencoder, eliminating the need for gradient-based optimization or additional training.
- Extensive experiments on eight SOTA or widely used generative models demonstrate that AEDR improves the attribution accuracy by an average of 25.5% and reduces the attribution time to just 1% of the best baseline.

2 Related Work

Image Generative Models. Early frameworks like Generative Adversarial Networks (GANs) (Goodfellow et al. 2014), Variational Autoencoders (VAEs) (Kingma and

Welling 2014), and autoregressive methods such as PixelCNN (Van Den Oord, Kalchbrenner, and Kavukcuoglu 2016) laid the groundwork for realistic image synthesis. However, diffusion models have recently become the leading approach. Denoising Diffusion Probabilistic Models (DDPMs) (Ho, Jain, and Abbeel 2020) achieve remarkable image fidelity by iteratively adding and reversing Gaussian noise, using simplified objectives and U-Net architectures. Building on this, Latent Diffusion Models (LDMs) improved efficiency by processing diffusion within a compact latent space, enabling rapid, high-resolution image generation with significantly lower computational requirements.

Detection of AI-Generated Images. As generative images grow increasingly photorealistic, the need for reliable detection is increasing (Chen, Fu, and Lyu 2023). Early work by Marra combined CycleGAN with steganalysis to identify GAN-generated images, laying a foundation for this field. Most existing methods frame the task as a binary classification problem, distinguishing between real and generated images. These approaches often rely on discriminative texture features (Chen and Yashtini 2024; Konstantinidou, Koutlis, and Papadopoulos 2025; Li et al. 2025) or frequency domain signals (Frank et al. 2020; Dong, Kumar, and Liu 2022; Corvi et al. 2023) as core detection cues. Recent approaches such as AEROBLADE (Ricker, Lukovnikov, and Fischer 2024) and HFI (Choi et al. 2024) adopt reconstruction losses via autoencoders and use LPIPS as a detection metric. Although these methods demonstrate promising performance in generative image detection, they do not address the more challenging task of origin attribution.

Origin Attribution of Generated Images. Current methods for attributing the origin of generated images can be broadly classified into three types: watermark-based methods (Swanson, Zhu, and Tewfik 1996; Wen et al. 2023; Yang et al. 2024, 2025), fingerprint-based methods (Ding, Thakur, and Li 2021; Yu, Davis, and Fritz 2019; Yu et al. 2020, 2021), and reconstruction-based methods (Wang et al. 2023, 2024). Watermark-based methods embed model-specific information into the generated image and retrieve this information during detection to identify the origin. Fingerprint-based methods inject unique patterns into the model during training and rely on dedicated classifiers for attribution. However, both active attribution approaches require additional intervention during image generation or model training and may compromise the quality of the generated images. In contrast, reconstruction-based passive methods enable origin attribution without the need for any extra operations. For example, both RONAN (Wang et al. 2023) and LatentTracer (Wang et al. 2024) adopt gradient-based reconstruction approaches, using the loss between the reconstructed and original images as the attribution signal.

3 Method

This section provides a detailed description of AEDR, the passive attribution method proposed in this paper. The process begins with two independent reconstructions of the input image using an autoencoder. The ratio of their reconstruction losses is then computed. To improve robustness,

this ratio is further calibrated using an image homogeneity metric, yielding the final attribution signal. The attribution outcome is determined by comparing this signal against a predefined threshold. The overall structure of the AEDR framework is depicted in Figure 3.

3.1 Problem Statement and Threat Models

We begin by formalizing the key concepts related to the attribution task, followed by the definition of the attribution goal and the specification of the threat model.

Belonging vs. Non-Belonging Image. Given an image generative model $\mathcal{M} : \mathcal{I} \rightarrow \mathcal{X}_{\mathcal{M}}$, where \mathcal{I} is the input space and $\mathcal{X}_{\mathcal{M}} \subset \mathcal{X}$ denotes the subset of images produced by \mathcal{M} , with \mathcal{X} representing the full image space. A test image x is classified as a belonging image if and only if $x \in \mathcal{X}_{\mathcal{M}}$; if $x \notin \mathcal{X}_{\mathcal{M}}$, it is classified as a non-belonging image.

Attribution Goal. The goal of the auditor is to determine whether a given image x was generated by the target model \mathcal{M} , without modifying the training or inference process of \mathcal{M} , and without applying any post-processing to its outputs. This is formulated as a binary function $F : \{\mathcal{M}, x\} \rightarrow \{0, 1\}$, where $F(\mathcal{M}, x) = 0$ indicates that x is attributed to \mathcal{M} , and $F(\mathcal{M}, x) = 1$ indicates a non-belonging image.

Threat Model. We assume a *white-box* setting in which the auditor has access only to the autoencoder \mathcal{R} associated with the model \mathcal{M} . Specifically, the auditor can query both the encoder and decoder for image reconstruction, but does not have access to model gradients, training data, or internal parameters of \mathcal{M} . This is in contrast to prior work, which require full white-box access, including gradient computation. By relying solely on reconstruction queries, AEDR is more practical for deployment in restricted-access scenarios.

3.2 Double-Reconstruction via Autoencoder

The specific workflow is as follows: Given the autoencoder \mathcal{R} of the target model \mathcal{M} and a test image x , we perform two successive reconstructions. The two reconstruction steps are respectively defined in Equations (1) and (2).

$$x^* = \mathcal{R}(x) = \mathcal{D}(\mathcal{E}(x)), \quad \mathcal{L}_1 = \mathcal{L}(x^*, x). \quad (1)$$

$$x^{**} = \mathcal{R}(x^*) = \mathcal{D}(\mathcal{E}(x^*)), \quad \mathcal{L}_2 = \mathcal{L}(x^{**}, x^*). \quad (2)$$

Here, x^* and x^{**} denote the reconstructed images obtained from the first and second passes through the autoencoder \mathcal{R} . The corresponding reconstruction losses are denoted by \mathcal{L}_1 and \mathcal{L}_2 , both computed using mean squared error (MSE). The advantage of using MSE is demonstrated in Experiment 4.5. AEDR focuses on analyzing the trend of variation in reconstruction losses for the test image x during the double-reconstruction process. Specifically, we define an uncalibrated attribution signal t as the ratio between the first and second reconstruction losses, formally given by:

$$t = \frac{\mathcal{L}_1}{\mathcal{L}_2} = \frac{\mathcal{L}(x^*, x)}{\mathcal{L}(x^{**}, x^*)}. \quad (3)$$

3.3 Calibration Mechanism

The inherent visual complexity of an image can significantly affect its reconstruction loss. Images with homogeneous backgrounds and low texture variation typically exhibit minimal differences in double-reconstruction losses.

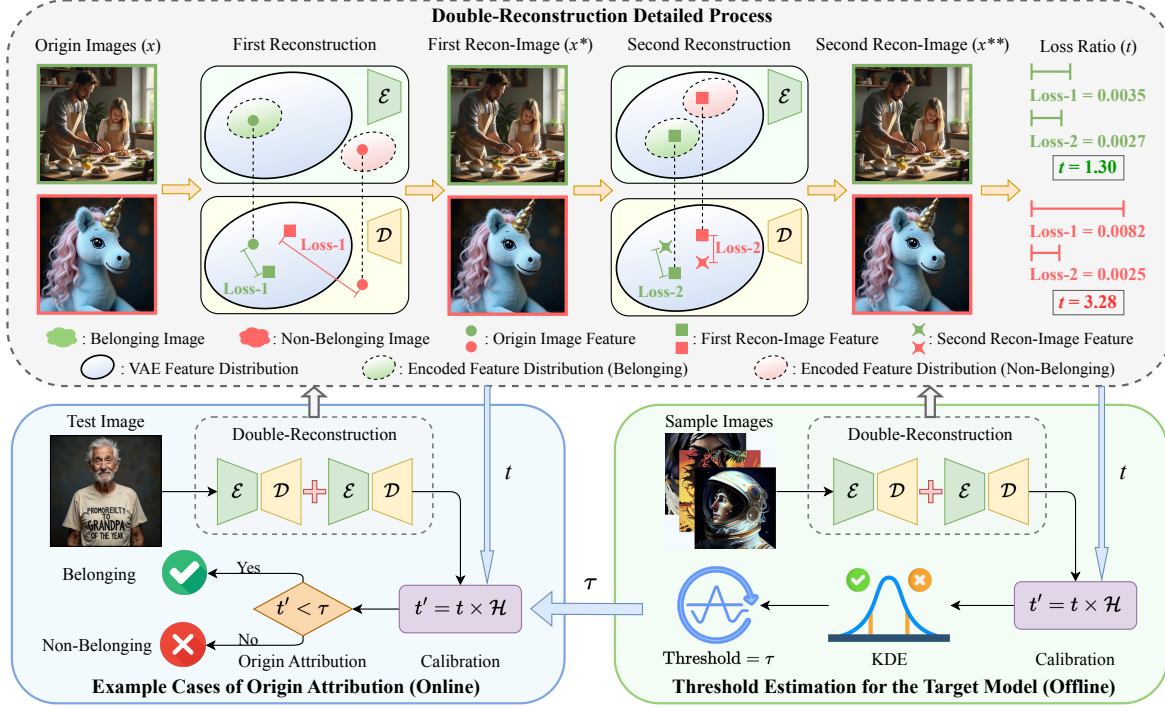


Figure 3: The framework of AEDR. Our method consists of three key modules: double-reconstruction based on autoencoder (Section 3.2), calibration mechanism (Section 3.3), and threshold determination via kernel density estimation (Section 3.4). AEDR employs the ratio of double-reconstruction losses, calibrated by an image homogeneity metric, as the attribution signal. The decision threshold is determined via kernel density estimation and applied for origin attribution.

In contrast, images containing complex textures or dynamic backgrounds often lead to substantial fluctuations in these losses (error examples see Technical Appendix, Section 6). To address this intrinsic bias, we introduce a homogeneity-aware loss calibration mechanism, defined as:

$$\mathcal{H} = \sum_{i=0}^{\ell-1} \sum_{j=0}^{\ell-1} \frac{P(i, j)}{1 + |i - j|}, \quad (4)$$

where $P(i, j)$ denotes the co-occurrence probability of grayscale levels i and j at a specified orientation and offset. The parameter ℓ represents the total number of grayscale levels (default value of 32 to ensure computational efficiency), and $|i - j|$ indicates the absolute difference in intensity between the corresponding pixel pairs. Based on this, the calibrated attribution signal is defined as follows:

$$t' = t \times \mathcal{H} = \frac{\mathcal{L}_1 \times \mathcal{H}}{\mathcal{L}_2}. \quad (5)$$

The calibrated metric t' effectively mitigates the intrinsic complexity bias in attribution assessment, thereby enhancing the overall attribution accuracy of AEDR.

3.4 Threshold Determination

Experimental results show that the calibrated attribution signal t' does not follow a consistent or well-defined probability distribution across different models (see Technical Appendix, Section 5), and may contain a small number of

outliers. To address this, we adopt kernel density estimation (KDE) (Kim and Scott 2012), a non-parametric method that makes no assumptions about the underlying distribution and is inherently robust to outliers. The attribution threshold is then derived from the cumulative distribution function (CDF) estimated via KDE, as defined by:

$$\tau = \inf \left\{ u \mid \int_{-\infty}^u \frac{1}{N h} \sum_{i=1}^N K\left(\frac{y - t'_i}{h}\right) dy \geq 1 - \alpha \right\}, \quad (6)$$

where N (set to 500 in our experiments) denotes the number of samples. Specifically, we estimate the distribution using 500 calibrated attribution signals obtained from belonging images. The parameter h represents the bandwidth of the kernel density estimation (Ruckthongsook et al. 2018), and K is the kernel function, for which a Gaussian kernel is used. The variable t'_i denotes the calibrated attribution signal of the i -th image. The quantity $1 - \alpha$ specifies the target cumulative probability for threshold selection. If the calibrated attribution signal $t' < \tau$, the x is classified as a belonging image; otherwise, it is considered a non-belonging image.

4 Experiments and Results

We begin by describing the experimental setup. Next, we assess the effectiveness and efficiency of AEDR in comparison to existing reconstruction-based passive attribution methods, specifically RONAN (Wang et al. 2023) and La-

\mathcal{M}_1	\mathcal{M}_2	RONAN						LatentTracer						AEDR							
		TP	FP	FN	TN	Acc	TP	FP	FN	TN	Acc	TP	FP	FN	TN	Acc	TP	FP	FN	TN	Acc
SD1.5	SD2.1	476	475	24	25	50.1%	475	62	25	438	91.3%	493	13	7	487	98.0%					
	SD2base	476	492	24	8	48.4%	475	415	25	459	93.4%	493	13	7	497	98.0%					
	SD3.5	476	460	24	40	51.6%	475	43	25	457	93.2%	493	3	7	497	99.0%					
	SDXL	476	491	24	9	48.5%	475	68	25	432	90.7%	493	10	7	490	98.3%					
	FLUX	476	484	24	16	49.2%	475	78	25	422	89.7%	493	12	7	488	98.1%					
	VQDM	476	499	24	1	47.7%	475	37	25	463	93.8%	493	5	7	495	98.8%					
SD2.1	KD2.1	476	471	24	29	50.5%	475	77	25	423	89.8%	493	4	7	496	98.9%					
	SD1.5	477	487	23	13	49.0%	476	244	24	256	73.2%	499	2	1	498	99.7%					
	SD3.5	477	408	23	92	56.9%	476	288	24	212	68.8%	499	8	1	492	99.1%					
	SDXL	477	500	23	0	47.7%	476	443	24	57	53.3%	499	1	1	499	99.8%					
	FLUX	477	480	23	20	49.7%	476	409	24	91	56.7%	499	4	1	496	99.5%					
	VQDM	477	499	23	1	47.8%	476	340	24	160	63.6%	499	0	1	500	99.9%					
SD2base	KD2.1	477	495	23	5	48.2%	476	372	24	128	60.4%	499	1	1	499	99.8%					
	SD1.5	475	409	25	91	56.6%	480	1	20	499	97.9%	499	11	1	489	98.8%					
	SD3.5	475	387	25	113	58.8%	480	4	20	492	97.2%	499	14	1	486	98.5%					
	SDXL	475	476	25	24	49.9%	480	9	20	491	97.1%	499	6	1	494	99.3%					
	FLUX	475	460	25	40	51.5%	480	28	20	472	95.2%	499	17	1	483	98.2%					
	VQDM	475	497	25	3	47.8%	480	5	20	495	97.5%	499	1	1	499	99.8%					
SD3.5	KD2.1	475	437	25	63	53.8%	480	30	20	470	95.0%	499	5	1	495	99.4%					
	SD1.5	479	500	21	0	47.9%	478	459	22	41	51.9%	490	7	10	493	98.3%					
	SD2.1	479	499	21	1	48.0%	478	486	22	14	49.2%	490	11	10	489	97.9%					
	SD2base	479	498	21	2	48.1%	478	489	22	11	48.9%	490	7	10	493	98.3%					
	SDXL	479	499	21	1	48.0%	478	500	22	0	47.8%	490	42	10	458	94.8%					
	FLUX	479	479	21	21	50.0%	478	500	22	0	47.8%	490	78	10	422	91.2%					
SDXL	VQDM	479	499	21	1	48.0%	478	492	22	8	48.6%	490	2	10	498	98.8%					
	KD2.1	479	467	21	33	51.2%	478	482	22	18	49.6%	490	22	10	478	96.8%					
	SD1.5	474	468	26	32	50.6%	478	227	22	273	75.1%	500	5	0	495	99.5%					
	SD2.1	474	469	26	31	50.5%	478	340	22	160	63.8%	500	3	0	497	99.7%					
	SD2base	474	494	26	6	48.0%	478	295	22	205	68.3%	500	6	0	494	99.4%					
	SD3.5	474	340	26	160	63.4%	478	292	22	208	68.6%	500	5	0	495	99.5%					
FLUX	FLUX	474	442	26	58	53.2%	478	421	22	79	55.7%	500	15	0	485	98.5%					
	VQDM	474	498	26	2	47.6%	478	349	22	151	62.9%	500	1	0	499	99.9%					
	KD2.1	474	484	26	16	49.0%	478	364	22	136	61.4%	500	2	0	498	99.8%					
	SD1.5	474	500	26	0	47.4%	478	407	22	93	57.1%	495	2	5	498	99.3%					
	SD2.1	474	499	26	1	47.5%	478	434	22	66	54.4%	495	9	5	491	98.6%					
	SD2base	474	497	26	3	47.7%	478	460	22	40	51.8%	495	6	5	494	98.9%					
VQDM	SD3.5	474	472	26	28	50.2%	478	465	22	35	51.3%	495	41	5	459	95.4%					
	SDXL	474	499	26	1	47.5%	478	476	22	24	50.2%	495	117	5	383	87.8%					
	FLUX	474	305	26	195	66.9%	478	462	22	38	51.6%	495	1	5	499	99.4%					
	KD2.1	474	469	26	31	50.5%	478	475	22	25	50.3%	495	27	5	473	96.8%					
	SD1.5	476	487	24	13	48.9%	477	390	23	110	58.7%	469	105	31	395	86.4%					
	SD2.1	476	472	24	28	50.4%	477	415	23	85	56.2%	469	94	31	406	87.5%					
KD2.1	SD2base	476	493	24	7	48.3%	477	402	23	98	57.5%	469	83	31	417	88.6%					
	SD3.5	476	463	24	37	51.3%	477	446	23	54	53.1%	469	31	31	469	93.8%					
	SDXL	476	490	24	10	48.6%	477	473	23	27	50.4%	469	50	31	450	91.9%					
	FLUX	476	473	24	27	50.3%	477	481	23	19	49.6%	469	37	31	463	93.2%					
	KD2.1	476	468	24	32	50.8%	477	421	23	79	55.6%	469	40	31	460	92.9%					
	SD1.5	481	483	19	17	49.8%	479	14	21	486	96.5%	472	157	28	343	81.5%					
Avg Acc	SD2.1	481	487	19	13	49.4%	479	40	21	460	93.9%	472	215	28	285	75.7%					
	SD2base	481	495	19	5	48.6%	479	24	21	476	95.5%	472	155	28	345	81.7%					
	SD3.5	481	497	19	3	48.4%	479	36	21	464	94.3%	472	146	28	354	82.6%					
	SDXL	481	493	19	7	48.8%	479	74	21	426	90.5%	472	188	28	312	78.4%					
	FLUX	481	493	19	7	48.8%	479	82	21	418	89.7%	472	159	28	341	81.3%					
	VQDM	481	497	19	3	48.4%	479	29	21	471	95.0%	472	50	28	450	92.2%					

Table 1: Results for distinguishing belonging images and images generated by other models.

Model	RONAN					LatentTracer					AEDR (ours)				
	TP	FP	FN	TN	Acc	TP	FP	FN	TN	Acc	TP	FP	FN	TN	Acc
SD1.5	476	481	24	19	49.5%	475	83	25	417	89.2%	493	6	7	494	98.7%
SD2.1	477	480	23	20	49.7%	476	417	24	83	55.9%	499	1	1	499	99.8%
SD2base	475	469	25	31	50.6%	480	29	20	471	95.1%	499	2	1	498	99.7%
SD3.5	479	393	21	107	58.6%	478	499	22	1	47.9%	490	15	10	485	97.5%
SDXL	474	479	26	21	49.5%	478	418	22	82	56.0%	500	3	0	497	99.7%
FLUX	474	370	26	130	60.4%	478	477	22	23	50.1%	495	25	5	475	97.0%
VQDM	476	473	24	27	50.3%	477	476	23	24	50.1%	469	44	31	456	92.5%
KD2.1	481	493	19	7	48.8%	479	83	21	417	89.6%	472	72	28	428	90.0%
Avg Acc	52.2%					66.7%					96.9%				

Table 2: Results for distinguishing belongings and real images. Real images are randomly selected from LAION-5B.

tentTracer (Wang et al. 2024). We then evaluate the generalization capability of AEDR across various autoencoder architectures. Finally, we perform ablation studies to examine the contribution of each component within AEDR.

4.1 Experimental Setup

Models. We evaluate AEDR on eight text-to-image Latent Diffusion Models, including five Stable Diffusion variants: SD1.5, SD2base, SD2.1, SDXL, and the latest SD3.5. We also include FLUX.1-dev (FLUX), which uses rectified flows. All models use Variational Autoencoders (VAE), except for two based on quantized autoencoders: Kandinsky 2.1 (KD2.1) with Modulating Quantized Vectors, and VQdiffusion (VQDM) using Vector Quantized VAE.

Dataset. We create a dataset of 9,000 images, comprising 1,000 real images sampled from LAION-5B (Schuhmann et al. 2022) and 8,000 AI-generated images. To minimize image diversity impact, we use the CLIP Interrogator (Pharmapsychotic 2023) to extract prompts from the real images. These prompts are then used to generate images with all eight models. The first 500 generated images are for hyperparameter tuning and threshold setting, while the remaining 500 are for performance evaluation. Further details are in Section 4 of the Technical Appendix.

4.2 Effectiveness

Distinguishing Belonging Images from Images Generated by Other Models. We compare our method against existing reconstruction-based passive attribution approaches, RONAN (Wang et al. 2023) and LatentTracer (Wang et al. 2024), to assess efficiency. All methods are tested on the same evaluation dataset across 8 models. For fair comparison, all baselines use official open source implementations.

The experimental results are shown in Table 1, where \mathcal{M}_1 represents the target model and \mathcal{M}_2 denotes other models. Our method achieves an average attribution accuracy of 95.1%, substantially outperforming RONAN and LatentTracer, which achieve 50.3% and 70.4%, respectively. While LatentTracer attains over 90% accuracy on models such as SD1.5, SD2base, and KD2.1, its performance degrades significantly on the remaining five models. The underlying reason is that when the target model is SD1.5, SD2base, and KD2.1, the reconstruction loss is on the order of 10^{-4} ,

whereas for stronger models such as FLUX, the reconstruction loss decreases to approximately 10^{-5} (see Figure 1 and Sections 1 to 3 of the Technical Appendix). And LatentTracer lacks any mechanism to calibrate the intrinsic complexity of images, resulting in substantial overlap between the distributions of belonging and non-belonging images, and thus a high false positive rate (FPR). These findings highlight the robustness of AEDR, which improves attribution accuracy by 24.7% over the strongest baseline.

Distinguishing Belonging Images from Real Images.

We further assess the ability of AEDR to distinguish belonging images from real images. As shown in Table 2, AEDR achieves an average accuracy of 96.9%, significantly outperforming RONAN (52.2%) and LatentTracer (66.7%). These results confirm that AEDR offers a substantial advantage—30.2% improvement over the best baseline. Notably, both baselines exhibit high FPR, whereas AEDR maintains a low FPR alongside its superior accuracy.

4.3 Efficiency

In this section, we evaluate the computational efficiency of our method. We test all 8 models with 1,000 images each, recording the average runtime for comparison. Due to memory constraints, we use `bf16` precision for FLUX and SD3.5, while the remaining six models are run with `fp32` precision. LatentTracer initializes gradient optimization using encoded representations of the input images, while RONAN uses random initialization and thus requires more optimization steps. Hence, our comparison focuses on LatentTracer as the more efficient baseline. As shown in Table 3,

Model	SD1.5	SD2.1	SD2base	SD3.5
LatentTracer	29.85s	92.09s	32.89s	29.85s
AEDR(ours)	0.27s	0.62s	0.25s	0.69s
Speedup	110.6×	148.5×	131.6×	43.3×
Model	SDXL	FLUX	VQDM	KD2.1
LatentTracer	162.94s	30.64s	12.58s	48.14s
AEDR(ours)	1.25s	0.68s	0.06s	0.39s
Speedup	130.4×	45.1×	209.7×	123.4×

Table 3: Running time on different models.

AEDR achieves an approximately **100 \times** speedup in runtime efficiency by replacing iterative gradient-based optimization with two simple forward passes through the autoencoder.

4.4 Generalization

We evaluate the generalization capability of AEDR across three distinct autoencoder architectures: VAE, VQ-VAE, and MoVQ. Table 4 shows that AEDR achieves an attribution accuracy exceeding 96% on VAE-based models. On VQ-VAE, the accuracy reaches 90.85%, and on MoVQ, it drops to 82.93%. The performance degradation primarily stems from the discrete nature of the latent space in quantized models. Specifically, the input tensor is mapped to the nearest latent code during quantization, introducing an error that hampers precise reconstruction and, consequently, fine-grained attribution. Despite this, AEDR outperforms LatentTracer on VQ-VAE. MoVQ remains a more challenging case, pointing to a promising direction for future research.

AE Type	Model	RONAN	LatentTracer	AEDR
VAE	SD1.5	49.44%	91.39%	98.45%
VAE	SD2.1	49.86%	61.70%	99.66%
VAE	SD2base	52.71%	96.43%	99.10%
VAE	SD3.5	49.98%	48.96%	96.70%
VAE	SDXL	51.48%	63.98%	99.50%
VAE	FLUX	52.26%	52.10%	96.65%
VQ-VAE	VQDM	49.86%	54.44%	90.85%
MoVQ	KD2.1	48.88%	93.13%	82.93%

Table 4: Generalization to different types of AE.

4.5 Ablation Studies

Impact of Reconstruction Loss Metric. We evaluate the effect of different reconstruction loss metrics on attribution accuracy using the Stable Diffusion v2-1. We utilized 500 belonging images and 500 randomly selected non-belonging images, including both generated and real images. Four commonly used metrics are compared: Mean Absolute Error (MAE), Mean Squared Error (MSE), Structural Similarity Index (SSIM), and Learned Perceptual Image Patch Similarity (LPIPS). As shown in Table 5, the attribution accuracies are 97.20% (MAE), 99.40% (MSE), 99.10% (SSIM), and 90.70% (LPIPS), respectively. Therefore, we adopt MSE as the default reconstruction loss metric in AEDR.

Metric	TP	FP	FN	TN	Acc
MAE	497	25	3	475	97.20%
MSE	496	2	4	498	99.40%
SSIM	495	4	5	496	99.10%
LPIPS	494	87	6	413	90.70%

Table 5: Results on different loss metrics.

Impact of Homogeneity Calibration. This section investigates the effect of homogeneity calibration in mitigating the influence of inherent image complexity on attribution accuracy. As reported in Table 6, homogeneity calibra-

tion leads to notable performance gains for most models, with improvements ranging from 0.18% to 9.09%. However, FLUX and VQDM (Zheng et al. 2022) exhibit slight decreases of 0.15% and 1.95%. Despite minor performance drops in a few cases, the overall advantage of the calibration mechanism clearly outweighs these limitations.

Model	w/o Calibration	w/ Calibration	Improvement
SD1.5	96.29%	98.45%	+2.16%
SD2.1	90.57%	99.66%	+9.09%
SD2base	93.71%	99.10%	+5.39%
SD3.5	94.97%	96.70%	+1.73%
SDXL	99.32%	99.50%	+0.18%
FLUX	96.80%	96.65%	-0.15%
VQDM	92.80%	90.85%	-1.95%
KD2.1	78.35%	82.93%	+4.58%

Table 6: Effects of homogeneity calibration.

Impact of Quantile Selection. This section investigates how different quantile selections affect attribution accuracy. Due to the significant variation in the distribution of attribution signals across models, we select model-specific quantile parameters. Each model is tested with 1,000 belonging images: 500 are used for threshold estimation, and the remaining 500 for evaluation. For each model, we select the value of α that yields the highest attribution accuracy on the estimation image set. These selected α values are summarized in Table 7; further details in Technical Appendix Section 5.

Model	Alpha	Estimation	Evaluation
SD1.5	0.015	98.67%	98.48%
SD2.1	0.003	99.73%	99.66%
SD2base	0.005	99.20%	98.90%
SD3.5	0.035	96.15%	96.70%
SDXL	0.003	99.29%	99.44%
FLUX	0.02	96.28%	96.65%
VQDM	0.085	90.47%	90.61%
KD2.1	0.05	83.47%	82.93%

Table 7: The Selection of quantile selection.

5 Conclusion

This paper addresses the critical challenges faced by current reconstruction-based attribution methods when dealing with state-of-the-art (SOTA) generative models. We propose AEDR (AutoEncoder Double Reconstruction), a novel, training-free passive attribution framework for AI-generated images. AEDR integrates a double-reconstruction scheme using an autoencoder with an effective calibration mechanism based on image homogeneity. By computing the reconstruction loss ratio over two consecutive reconstructions, AEDR efficiently mitigates biases arising from inherent image complexity, resulting in significantly improved attribution performance. Extensive experiments demonstrate that AEDR delivers a 25.5% relative improvement in attribution accuracy while achieving an approximately 100 \times speedup in inference time compared to leading baseline methods.

Acknowledgements

This work was supported in part by the National Natural Science Foundation of China under Grant 62472398, U2336206, 62121002, 62402469 and 62302146, and by the Fundamental Research Funds of a State Key Laboratory under CBCT2024KF01.

References

Batifol, S.; Blattmann, A.; Boesel, F.; Consul, S.; Diagne, C.; Dockhorn, T.; English, J.; English, Z.; Esser, P.; Kulal, S.; et al. 2025. FLUX. 1 Kontext: Flow Matching for In-Context Image Generation and Editing in Latent Space. *arXiv e-prints*, arXiv-2506.

Betker, J.; Goh, G.; Jing, L.; Brooks, T.; Wang, J.; Li, L.; Ouyang, L.; Zhuang, J.; Lee, J.; Guo, Y.; et al. 2023. Improving image generation with better captions. *Computer Science*. <https://cdn.openai.com/papers/dall-e-3.pdf>, 2(3): 8.

Carlini, N.; Hayes, J.; Nasr, M.; Jagielski, M.; Sehwag, V.; Tramer, F.; Balle, B.; Ippolito, D.; and Wallace, E. 2023. Extracting training data from diffusion models. In *32nd USENIX Security Symposium (USENIX Security 23)*, 5253–5270.

Chen, C.; Fu, J.; and Lyu, L. 2023. A pathway towards responsible ai generated content. *arXiv preprint arXiv:2303.01325*.

Chen, D.; Yu, N.; Zhang, Y.; and Fritz, M. 2020. Gan-leaks: A taxonomy of membership inference attacks against generative models. In *Proceedings of the 2020 ACM SIGSAC conference on computer and communications security*, 343–362.

Chen, Y.; and Yashtini, M. 2024. Detecting AI Generated Images Through Texture and Frequency Analysis of Patches. In *2024 4th International Conference on Artificial Intelligence, Virtual Reality and Visualization*, 103–110. IEEE.

Choi, S.; Park, S.; Lee, J.; Kim, S.; Choi, S. J.; and Lee, M. 2024. HFI: A unified framework for training-free detection and implicit watermarking of latent diffusion model generated images. *arXiv preprint arXiv:2412.20704*.

Corvi, R.; Cozzolino, D.; Poggi, G.; Nagano, K.; and Verdoliva, L. 2023. Intriguing properties of synthetic images: from generative adversarial networks to diffusion models. In *Proceedings of the IEEE/CVF conference on computer vision and pattern recognition*, 973–982.

Dhariwal, P.; and Nichol, A. 2021. Diffusion models beat gans on image synthesis. *Advances in neural information processing systems*, 34: 8780–8794.

Ding, Y.; Thakur, N.; and Li, B. 2021. Does a GAN leave distinct model-specific fingerprints? In *BMVC*, 22.

Dong, C.; Kumar, A.; and Liu, E. 2022. Think twice before detecting gan-generated fake images from their spectral domain imprints. In *Proceedings of the IEEE/CVF conference on computer vision and pattern recognition*, 7865–7874.

Esser, P.; Kulal, S.; Blattmann, A.; Entezari, R.; Müller, J.; Saini, H.; Levi, Y.; Lorenz, D.; Sauer, A.; Boesel, F.; et al. 2024. Scaling rectified flow transformers for high-resolution image synthesis. In *Forty-first international conference on machine learning*.

Frank, J.; Eisenhofer, T.; Schönherr, L.; Fischer, A.; Kolossa, D.; and Holz, T. 2020. Leveraging frequency analysis for deep fake image recognition. In *International conference on machine learning*, 3247–3258. PMLR.

Goodfellow, I. J.; Pouget-Abadie, J.; Mirza, M.; Xu, B.; Warde-Farley, D.; Ozair, S.; Courville, A.; and Bengio, Y. 2014. Generative adversarial nets. *Advances in neural information processing systems*, 27.

Ho, J.; Jain, A.; and Abbeel, P. 2020. Denoising diffusion probabilistic models. *Advances in neural information processing systems*, 33: 6840–6851.

Kim, J.; and Scott, C. D. 2012. Robust kernel density estimation. *The Journal of Machine Learning Research*, 13(1): 2529–2565.

Kingma, D. P.; and Welling, M. 2014. Auto-Encoding Variational Bayes. In Bengio, Y.; and LeCun, Y., eds., *2nd International Conference on Learning Representations, ICLR 2014, Banff, AB, Canada, April 14-16, 2014, Conference Track Proceedings*.

Konstantinidou, D.; Koutlis, C.; and Papadopoulos, S. 2025. Texturecrop: Enhancing synthetic image detection through texture-based cropping. In *Proceedings of the Winter Conference on Applications of Computer Vision*, 1459–1468.

Li, B.; Wei, Y.; Fu, Y.; Wang, Z.; Li, Y.; Zhang, J.; Wang, R.; and Zhang, T. 2024. Towards reliable verification of unauthorized data usage in personalized text-to-image diffusion models. *arXiv preprint arXiv:2410.10437*.

Li, J.; Jiang, W.; Shen, L.; and Ren, Y. 2025. Optimized Frequency Collaborative Strategy Drives AI Image Detection. *IEEE Internet of Things Journal*.

Luo, L.; Chen, Z.; Chen, M.; Zeng, X.; and Xiong, Z. 2009. Reversible image watermarking using interpolation technique. *IEEE Transactions on information forensics and security*, 5(1): 187–193.

Ong, D. S.; Chan, C. S.; Ng, K. W.; Fan, L.; and Yang, Q. 2021. Protecting intellectual property of generative adversarial networks from ambiguity attacks. In *Proceedings of the IEEE/CVF Conference on Computer Vision and Pattern Recognition*, 3630–3639.

Pharmapsychotic. 2023. Clip-interrogator. <https://github.com/pharmapsychotic/clip-interrogator>. Accessed: 2025-11-26.

Podell, D.; English, Z.; Lacey, K.; Blattmann, A.; Dockhorn, T.; Müller, J.; Penna, J.; and Rombach, R. 2023. Sdxl: Improving latent diffusion models for high-resolution image synthesis. *arXiv preprint arXiv:2307.01952*.

Razzhigaev, A.; Shakhmatov, A.; Maltseva, A.; Arkhipkin, V.; Pavlov, I.; Ryabov, I.; Kuts, A.; Panchenko, A.; Kuznetsov, A.; and Dimitrov, D. 2023. Kandinsky: an improved text-to-image synthesis with image prior and latent diffusion. *arXiv preprint arXiv:2310.03502*.

Ricker, J.; Lukovnikov, D.; and Fischer, A. 2024. Aeroblade: Training-free detection of latent diffusion images using autoencoder reconstruction error. In *Proceedings of the IEEE/CVF Conference on Computer Vision and Pattern Recognition*, 9130–9140.

Rombach, R.; Blattmann, A.; Lorenz, D.; Esser, P.; and Ommer, B. 2022. High-resolution image synthesis with latent diffusion models. In *Proceedings of the IEEE/CVF conference on computer vision and pattern recognition*, 10684–10695.

Ruckthongsook, W.; Tiwari, C.; Oppong, J. R.; and Natesan, P. 2018. Evaluation of threshold selection methods for adaptive kernel density estimation in disease mapping. *International Journal of Health Geographics*, 17: 1–13.

Schuhmann, C.; Beaumont, R.; Vencu, R.; Gordon, C.; Wightman, R.; Cherti, M.; Coombes, T.; Katta, A.; Mullis, C.; Wortsman, M.; et al. 2022. Laion-5b: An open large-scale dataset for training next generation image-text models. *Advances in neural information processing systems*, 35: 25278–25294.

Swanson, M. D.; Zhu, B.; and Tewfik, A. H. 1996. Transparent robust image watermarking. In *Proceedings of 3rd IEEE International Conference on Image Processing*, volume 3, 211–214. IEEE.

Van Den Oord, A.; Kalchbrenner, N.; and Kavukcuoglu, K. 2016. Pixel recurrent neural networks. In *International conference on machine learning*, 1747–1756. PMLR.

Wang, Z.; Chen, C.; Zeng, Y.; Lyu, L.; and Ma, S. 2023. Where Did I Come From? Origin Attribution of AI-Generated Images. In *Thirty-seventh Conference on Neural Information Processing Systems*.

Wang, Z.; Sehwag Vikash, C.; Chen; Lyu, L.; Metaxas, D. N.; and Ma, S. 2024. How to Trace Latent Generative Model Generated Images without Artificial Watermark? In *International Conference on Machine Learning*.

Wen, Y.; Kirchenbauer, J.; Geiping, J.; and Goldstein, T. 2023. Tree-ring watermarks: Fingerprints for diffusion images that are invisible and robust. *arXiv preprint arXiv:2305.20030*.

Yang, Z.; Zeng, K.; Chen, K.; Fang, H.; Zhang, W.; and Yu, N. 2024. Gaussian shading: Provable performance-lossless image watermarking for diffusion models. In *Proceedings of the IEEE/CVF Conference on Computer Vision and Pattern Recognition*, 12162–12171.

Yang, Z.; Zhang, X.; Chen, K.; Zeng, K.; Yao, Q.; Fang, H.; Zhang, W.; and Yu, N. 2025. Gaussian Shading++: Rethinking the Realistic Deployment Challenge of Performance-Lossless Image Watermark for Diffusion Models. *arXiv preprint arXiv:2504.15026*.

Yu, N.; Davis, L. S.; and Fritz, M. 2019. Attributing fake images to gans: Learning and analyzing gan fingerprints. In *Proceedings of the IEEE/CVF international conference on computer vision*, 7556–7566.

Yu, N.; Skripniuk, V.; Abdelnabi, S.; and Fritz, M. 2021. Artificial fingerprinting for generative models: Rooting deepfake attribution in training data. In *Proceedings of the IEEE/CVF International conference on computer vision*, 14448–14457.

Yu, N.; Skripniuk, V.; Chen, D.; Davis, L.; and Fritz, M. 2020. Responsible disclosure of generative models using scalable fingerprinting. *arXiv preprint arXiv:2012.08726*.

Zhao, H.; Zhou, W.; Chen, D.; Wei, T.; Zhang, W.; and Yu, N. 2021. Multi-attentional deepfake detection. In *Proceedings of the IEEE/CVF conference on computer vision and pattern recognition*, 2185–2194.

Zheng, C.; Vuong, T.-L.; Cai, J.; and Phung, D. 2022. Movq: Modulating quantized vectors for high-fidelity image generation. *Advances in Neural Information Processing Systems*, 35: 23412–23425.